Effects of short-range order on phase equilibria and opto-electronic properties of ternary alloy $Zn_xCd_{1-x}Te$

B.B. Dumre, R.J. Ellingson, S.V. Khare [*]

Department of Physics and Astronomy, and Wright Center for Photovoltaics Innovation and Commercialization (PVIC), University of Toledo, Toledo, OH, 43606, USA

ABSTRACT

We employ first principles methods based on density functional theory and beyond to study $Zn_xCd_{1-x}Te$, $0 \leq x \leq 1$, alloys in the zinc blende (B3) crystal structure. Cluster Expansion and Monte Carlo formalisms were deployed to provide a phase diagram determining consolute temperature of 387 K at 40% Zn concentration. Opto-electronic properties are computed with the hybrid HSE06 functional for disordered $Zn_xCd_{1-x}Te$ alloys, which were simulated using special quasi-random structures. Bowing effects in the bandgap and effective carrier masses were observed in alloying which can be attributed to local geometrical distortions as portrayed by bond length distributions. Downward bowing in the electronic bandgap will be beneficial in photovoltaic applications through increased net photocurrent. Absorption coefficients show robust absorption in $Zn_xCd_{1-x}Te$ as indicated by substantial optical absorption throughout all Zn concentrations, aided by low reflectivity that ensures a high absorption. Presence of short-range order in $Zn_{0.25}Cd_{0.75}Te$ was observed through clustering and anti-clustering among different cationic species of Zn and Cd. It has a value of 0.11 at 1000 K compared to -0.79 at 400 K. The bandgap of $Zn_{0.25}Cd_{0.75}Te$ at 1000 K was found to be slightly higher, 0.05 eV, than at 400 K, consistent with the value of short-range order. Thus, short-range order and possibly composition can be used in the design and synthesis of the appropriate solar cell, thereby improving the performance in this system.

1. Introduction

CdTe based solar cells are the most successful thin film technology commercially due to their record high efficiency of 22.1% [1], reliability and low-cost production methods [2,3]. However, this efficiency value is still far from the Shockley-Queisser (SQ) limit of 30% [4]. The open-circuit voltage (V_{OC}), one of the factors contributing to efficiency, obtained so far is 880 mV, which is only 76.1% of the SQ limit of 1157 mV [1,4]. In contrast, the V_{OC} of some other representative materials such as GaAs have been observed to be 97.7% of the SQ limit [5]. In order to ascend the SQ curve for a better V_{OC}, this issue has been addressed by tuning the bandgap of CdTe by alloying with CdS [6–8], CdSe [9–11] or ZnTe [2,12–16]. Out of these options, the lattice mismatch in between CdS and CdTe is about 10% [7] in comparison to CdSe and ZnTe, where both have around 6% lattice mismatch with CdTe [17,18]. Such a large lattice mismatch in CdS causes low dopant solubility which in turn increases carrier recombination rates due to a high defect density [19,20]. Furthermore, parasitic absorption in CdS in wavelength range 300–500 nm reduces net photo-current [8].

Moreover, the lower V_{OC} in CdTe is also attributed towards lower carrier lifetime [21–23]. The carrier lifetimes are curbed by recombination brought about by the defects [24,25], which frequently exist in high proportion at the front- and back-contact interfaces necessary to collect electrons and holes. Alloying CdTe with CdSe or ZnTe has been seen as a defect minimizing process and subsequent increase in carrier lifetime, radiative efficiency and short-circuit current density [10,11,26]. Also, as CdSe and CdS are thermodynamically synthesized in either zinc blende or wurtzite phases [27], the synthesis of ZnTe and its alloys with CdTe only in zinc blende structure [13] poses an ease in the synthesis process. All these efforts in reaching the SQ limit has stalled in recent years because the SQ limit mainly adheres to radiative recombination losses, whereas electrical and optical losses are primarily diminishing the potential [28]. Instead, tandem solar cell configurations are seen to surpass SQ limit of single-junction solar cells [28]. Thus, $Zn_xCd_{1-x}Te$ has been used in a tandem configuration also because it has a tunable bandgap from 1.4 eV to 2.26 eV [14]. Besides this, inserting a wide bandgap material between the absorber layer and the metal contact has delivered in an increase in efficiency [29–31]. Especially, $Zn_xCd_{1-x}Te$ with higher

---

Zn concentrations can be used as a wide bandgap material. Its negligible valence band discontinuity with respect to CdTe does not resist hole transfer whereas a large conduction band offset, in principle, reflects electrons back toward the front contact to CdTe, minimizing minority carrier recombination losses at metal-back contact interface [32,33]. Besides solar cells, the $Zn_xCd_{1-x}Te$ alloy system has seen usage in switching devices, light emitting diodes, X-ray detectors, γ-ray detectors, photorefractive gratings, etc. [34–36].

Significant attention has been provided both theoretically [12,37, 38] and experimentally [2,14,15] to comprehend the properties and applications of the $Zn_xCd_{1-x}Te$ system. However, a panoptic computational view of its structure emphasizing especially on the property of the disordered alloy and its effects on the opto-electronic properties has been missing. Therefore, in this study, we have investigated detailed structural, energetic, thermodynamic, and opto-electronic properties of $Zn_xCd_{1-x}Te$ alloy system. Using Cluster Expansion (CE) [39–42] and Monte Carlo (MC) [43–47] formalisms, we have characterized phase stability of $Zn_xCd_{1-x}Te$ determining that the solubility can be achieved at 40% Zn concentration above 387 K temperature. Miscibility gap below this temperature has been attributed to the strain due to the accommodation of two different atoms Zn and Cd of differing covalent radii shown by the bond length distribution. This bond length variation also causes a downward bowing behavior in bandgap, thereby reducing the bandgap values in the intermediate members of the alloy. The reduction in their values meets the SQ limit and causes an increment in photovoltaic efficiency. Good agreement of our calculated values with the experimental data is observed. The analysis of short-range order gives us some insight into the bandgap engineering of the material. Sustained absorption and low optical reflectivity make $Zn_xCd_{1-x}Te$ alloy system a better solar material.

2. Computational methods

All the density functional theory (DFT) calculations were performed using the Vienna Ab initio Simulation Package (VASP) [48–51] with Projector Augmented Wave (PAW) method [52,53] and Generalized Gradient Approximation (GGA) exchange-correlation functional prescribed by Perdew-Burke-Ernzerhof (PBE) [54,55]. PAW PBE pseudopotentials from the VASP library [48–51], including only the outer-core electrons as valence electrons, were used for Zn, Cd and Te. In the convergence trial with respect to energy, a cutoff of 500 eV was selected to be used for the plane-wave basis set [56–59]. Calculations were carried out on Γ-centered k-point meshes comprising of 4000 k-points per reciprocal atom (KPPRA) [60–64]. Electronic minimizations with a convergence criterion of 10^{-6} eV/atom were performed using Gaussian smearing of width 0.05 eV [65–69]. Initial crystal structures of materials used in this work were taken from the Materials Project [70] and geometrically optimized until forces acting on each atom were less than 0.01 eV/Å as mentioned in earlier work [71–76].

Accurate ground state energies of the reactants and products are calculated, using high precision static calculations, in order to compute formation energy [77–80]. Formation energy per formula unit of $Zn_xCd_{1-x}Te$ is calculated as:

$$\Delta E_f(x) = E(Zn_xCd_{1-x}Te) - xE(Zn) - (1-x)E(Cd) - E(Te) \quad (1)$$

where E(Zn), E(Cd), E(Te) are the ground state energies of zinc (Space Group: $P6_3/mmc$), cadmium (Space Group: $P6_3/mmc$) and tellurium (Space Group: $P3_121$) in solid states, respectively.

Formation energy landscapes and phase diagrams of ZnTe–CdTe were calculated using cluster expansion formalism [81] deploying MIT Ab initio Phase Stability (maps) code from the Alloy Theoretic Automated Toolkit (ATAT) [82–85]. Stiffness versus length relationships [86, 87] were utilized to calculate vibrational contributions to the free energy among 5 unique structures in the set enumerated by cluster expansion. For each structure, perturbations of magnitude 0.2 Å at 3

separate volumes were tested to obtain dynamical matrices, phonon spectra, and vibrational free energies. This information obtained using the fitsvsl and svsl codes in ATAT [82–85] was used in modifying the corresponding phase boundaries. Special Quasirandom Structures (SQSs) [88], utilized to calculate random Zn/Cd occupation occurring above the predicted consolute temperature, were generated using the sqs2tdb code within ATAT [82–85]. To simulate credible random configurations, $Zn_xCd_{1-x}Te$ SQSs were constructed from $2 \times 2 \times 2$ supercells of the conventional zinc blende (B3) unit cells at concentrations of x = 0.25, 0.50, and 0.75.

Due to the self-interaction error, bandgaps and absorption onsets are underestimated by standard exchange-correlation functionals, e.g., GGA and local density approximation (LDA) [89,90]. Hence, we employed the Heyd-Scuseria-Ernzerhof hybrid functional (HSE06) [91–93] to calculate the optoelectronic properties of $CdSe_xTe_{1-x}$. The HSE06 functional including 25% of the exact exchange from Hartree-Fock theory along with 75% of the exchange from GGA has been shown to give significantly improved agreement with experiment for semiconductors and insulators [94,95]. Using this method, for which the exact exchange was treated on a coarser grid of 2000 KPPRA to conserve computational resources [9,96], we calculated the electronic density of states (DOS) and frequency-dependent complex dielectric function ($\varepsilon_1 + i\varepsilon_2$) for each compound, including both end members and SQSs. From the latter values, derived optical properties such as absorption coefficient and reflectivity were determined implementing the corresponding modules in pymatgen [97]. Such derived absorption coefficient is utilized to calculate Urbach energy [98,99]. To gain further insight into the optoelectronic properties, effective masses (m^*) of electrons and holes were calculated using the BoltzTrap2 [100,101] package where we have considered the calculations in room temperature (300 K) with constant relaxation time approximated to be 10^{-14} s. Besides the single band at both Valence Band Maximum (VBM) and Conduction Band Minimum (CBM), other bands or band-branches within 1.5 eV of range on either side of the mid-bandgap were also considered for interpolation of bands while calculating the effective masses. The calculated effective masses are further utilized to calculate charge carrier mobilities [102], where the relaxation time is approximated to be 10^{-14} s. Along with dielectric constant at high-frequency limit (ε_∞), we have again utilized effective masses to compute exciton binding energy [102,103].

To investigate short-range order (SRO) effects occurring in the Zn/Cd sublattice of $Zn_xCd_{1-x}Te$ structures for which no long-range order exists, we focus on the relevant concentration of x = 0.25. Here, Monte Carlo simulations are performed on 1728-atom supercells using the Easy Monte Carlo Code (emc2) within ATAT [82–85]. As the consolute temperature of 387 K is predicted including the vibrational contribution to the phase equilibrium, we test $Zn_{0.25}Cd_{0.75}Te$ at temperatures ranging from 400 K to 1000 K, in steps of 50 K. We engage two techniques of analysis to determine the degree of short-range order present within each structure. First, we compare the distribution of Zn–Cd coordination values, occurring throughout all sites at 400 K and 1000 K, with the corresponding values of a completely disordered configuration. Secondly, we define the following short-range order parameter for Zn–Cd pairs [104]:

$$\sigma(T) = 1 - \left[\left(1 - N^{Zn-Cd}(T) / N_{random}^{Zn-Cd} \right) / \left(1 - N_{ordered}^{Zn-Cd} / N_{random}^{Zn-Cd} \right) \right] \quad (2)$$

where N^{Zn-Cd}, $N_{ordered}^{Zn-Cd}$, and N_{random}^{Zn-Cd} represent the number of Zn–Cd bonds in the configuration simulated at some intermediate temperatures (T = 400 K, 1000 K), the ordered configuration (with each Te coordinated to an equal number of Zn and Cd atoms) at absolute zero temperature, and the completely random configuration approached at very high temperatures (T≫1000 K) in $Zn_{0.25}Cd_{0.75}Te$. Here, the positive and negative values of σ (max. +1 or −1) correspond to additional or reduced Zn–Cd bonds relative to the random limit, and hence a value of zero implies complete disorder.

To provide further insight into electronic structure, we have

performed calculations of Crystal Orbital Hamiltonian Populations (COHP) and effective charges using the LOBSTER package [105–108] and Bader analysis [109–112] respectively.

3. Results

3.1. Properties of cation-disordered $Zn_xCd_{1-x}Te$

ZnTe and CdTe in the solid state are most stable in B3 crystal structure as also their alloys $Zn_xCd_{1-x}Te$ [13]. The end members, ZnTe and CdTe, of the alloy $Zn_xCd_{1-x}Te$ have cations in 4a and anions in 4d Wyckoff positions. There are two different atoms in the cationic sublattice of 4a Wyckoff positions. Thus, the intermediate members of the alloy have cationic disorder. The SQSs of cation disordered supercells have 64 atoms in each cell for the intermediate members of the alloy $Zn_xCd_{1-x}Te$ for x = 0.25, 0.50 and 0.75. The coordination number is 4 as observed ubiquitously in B3 structure with tetrahedral geometry and ABCABC … layer stacking. Since we want to study various properties of cation-disordered $Zn_xCd_{1-x}Te$ as a function of concentration, let's first define a bowing parameter (δ_p). It helps us to understand the deviation from linearity for any physical quantity (p) such as, lattice constant (a), bandgap (E_g), effective mass (m^*), or others, as [113]:

$$p_{mix}(x_{Zn}) = x_{Zn}p_{ZnTe} + (1 - x_{Zn})p_{CdTe} - x_{Zn}(1 - x_{Zn})\delta_p, \qquad (3)$$

where x_{Zn} is the percentage of Zn in the alloy and, p_{mix}, p_{ZnTe} and p_{CdTe} are values of the physical quantity associated with resultant alloy, ZnTe and CdTe respectively.

Table S1 displays calculated equilibrium lattice constant, volume, and formation energy of the $Zn_xCd_{1-x}Te$ alloy system. Our computed lattice constant matches closely with previous theoretical [114,115] and experimental [116–118] work. We have found that the bowing parameter for lattice constant δ_a is −0.06 Å, using Eq. (3) with p = a. Such a small bowing parameter suggests that the lattice constant for this system roughly follows Vegard's law [119]. Further, the unit cell volumes are found to decrease with average slopes of 13.52 Å^3 per formula unit per concentration (x). This contraction in volume can be attributed to the increment in Zn concentration whose volume is smaller than Cd in this tetrahedrally coordinated covalent environment [120]. Also, the bowing parameter for formation energy $\delta_{\Delta E_f}$ is −78.08 meV, obtained using Eq. (3) with p = ΔE_f. Thus, there is an increase in formation energy for the intermediate members of the alloy. This endothermicity is because of the strain in accommodating two different atoms Zn and Cd of different covalent radii, 130.4 p.m. and 148.2 p.m. respectively. The effect is more pronounced in $Zn_{0.50}Cd_{0.50}Te$ [121]. Moreover, these results of formation energy and lattice constants have been graphically displayed in Figure S1, where there is a clear bowing in formation energy whereas the lattice constant curve is nearly a straight line.

To understand the internal geometrical structure in the alloy, we have presented the first nearest neighbor bond length distribution in Figure S2. The anticipated distortion in the cation-Te tetrahedra due to the cation disorder has been exhibited by the corresponding deviations in the ideal bond lengths. Particularly, the first nearest neighbor bond lengths of attractive type, viz. Cd–Te and Zn–Te are calculated to be 2.87 Å and 2.68 Å respectively in the end members. However, all the Cd–Te median values (shown by red lines in the box and whisker plots in Figure S2) in all the intermediate members are lower than in the end member CdTe. Similarly, all the Zn–Te median values in all the intermediate members are higher than in the end member ZnTe. In the case of x = 0.50, our calculated values of the median bond lengths in Cd–Te and Zn–Te of respectively 2.85 Å and 2.70 Å are matching closely with the experimental results of respectively 2.78 Å and 2.66 Å [122]. Also, the distribution of these (Cd–Te and Zn–Te) bond lengths is nearly 0.07 Å wide in all the intermediate members. Similarly, the other nearest neighbor bond lengths of repulsive type, viz. Zn–Zn, Zn–Cd, Cd–Cd and Te–Te have much wider distribution (0.30–0.53) Å. Moreover, the first

nearest bond lengths Zn–Zn and Te–Te in ZnTe end member are both same and equal to 4.37 Å, whereas Cd–Cd and Te–Te in CdTe end member are both same and equal to 4.86 Å. Similar to the effect observed in the case of Cd–Te and Zn–Te bond lengths as discussed earlier in this paragraph, the Zn–Zn median bond lengths decreased whereas Cd–Cd median bond lengths increased in all the intermediate alloys. The Te–Te and Zn–Cd first nearest median bond lengths are distributed throughout the bond lengths of Cd–Cd, Zn–Zn and Te–Te in the end members. Although all the participating atoms in the bond length pairs discussed are the same in either end members or the intermediate members of the alloys, the altercation in the bond lengths can be correlated to the presence of the type of cation in the nearest tetrahedra or the second and further nearest neighbor cation type. The increment of zinc in the neighborhood created an increase in the Zn–Zn and Zn–Te bond lengths whereas reduction in the Cd–Cd and Cd–Te bond lengths. This is because the difference in electronegativity in Zn–Te bond is lower than in Cd-Te [123] which makes the former pair of bonds weaker than the latter. Thus, Cd–Te becomes more attractive in the intermediate members and causes the bond length to shrink whereas Zn–Te bond length increases due to lesser bonding strength and occupies the vacant space in the neighborhood created by the shrinkage of Cd–Te tetrahedra. Furthermore, the distortion is the highest in $Zn_{0.50}Cd_{0.50}Te$ and all the bond lengths are much widely distributed, owing to the strain due to two differing cation sizes [121] as discussed in the previous paragraph and a perfectly random distribution of the tetrahedra. Therefore, there is a stark variation in the bond lengths when compared to their pairs in the end members. Hence, we can say that the disorder caused such difference in the bond lengths in the alloys. Further implications of the varying bond lengths in opto-electronic properties and short-range order of the material will be discussed later in this section and section 3.3 respectively.

The disorder in the cationic positions of $Zn_xCd_{1-x}Te$ alloy also has a major impact on its electronic properties. The exact values of bandgaps of $Zn_xCd_{1-x}Te$, are reported in Table S2. The values calculated using HSEO6 pseudopotential for the end members CdTe and ZnTe are 1.54 eV and 2.39 eV which closely match the experimental values of 1.50 eV [124] and 2.39 eV [125,126] respectively in contrast with earlier theoretical work. All the bandgaps for the alloy members calculated are direct in nature at the Γ(0,0,0) k-point. Our more accurate match with experimental results may be attributed to the difference in pseudopotentials used in earlier theoretical work. Reshak et al. obtained the bandgap of 1.31 eV for CdTe using Engel-Vosko (EV)-GGA [127] whereas Huang et al. obtained the bandgap of 2.24 eV for ZnTe using LDA [114] pseudopotentials. Our results calculated using GGA are also provided for comparison which exhibit similar mismatch with experimental results.

A bowing effect is present in the values of bandgaps of intermediate members of $Zn_xCd_{1-x}Te$ which has been graphically displayed in Fig. 1a. The bowing parameter of bandgaps δ_{E_g} is 1.63 eV, obtained using Eq. (3) with p = E_g. This bowing trend can be attributed to the local distortions arising in the disordered solid solution [128]. We have already analyzed the distribution of the bond length (Figure S2) in the alloy due to the differing cation types in the third paragraph of this section. Due to this bond length distribution, charge distribution segregates correspondingly among the alloy bonds that initiates the bowing behavior of the bandgaps [129]. The downward bowing effect brings the bandgap to a minimum of 1.49 eV in $Zn_{0.25}Cd_{0.75}Te$. As this value of the bandgap is near to the ideal value of 1.4 eV for a photovoltaic absorber according to the SQ limit [4], $Zn_{0.25}Cd_{0.75}Te$ (shown in Fig. 2) is proposed to be beneficial for optimal efficiency of energy absorption. Also, since the bandgap of $Zn_xCd_{1-x}Te$ alloy system spans from infrared to the visible range of the electromagnetic-spectrum, the other members of the $Zn_xCd_{1-x}Te$ alloy system can be used as graded absorber layers in order to capture the entire solar spectrum. Besides the dependence of bandgap on the concentration of Zn, quantum confinement may be used as another tuning parameter, as the bandgap has been observed to vary
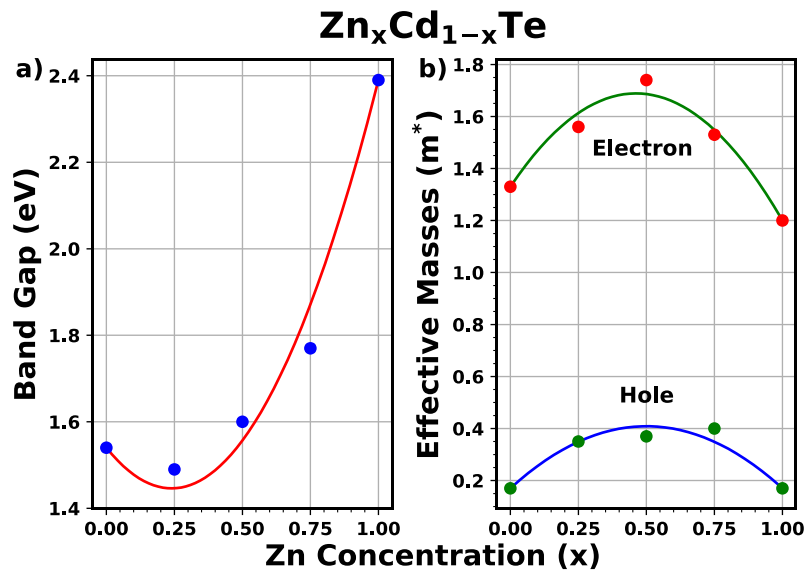
Fig. 1. a) Electronic bandgaps, and b) effective masses of $Zn_xCd_{1-x}Te$ alloys in B3 crystal structure calculated using the hybrid HSEO6 functional. Here, points appear for calculated data whereas curves sketch fitting based on a bowing parameter as defined in Eq. (3).
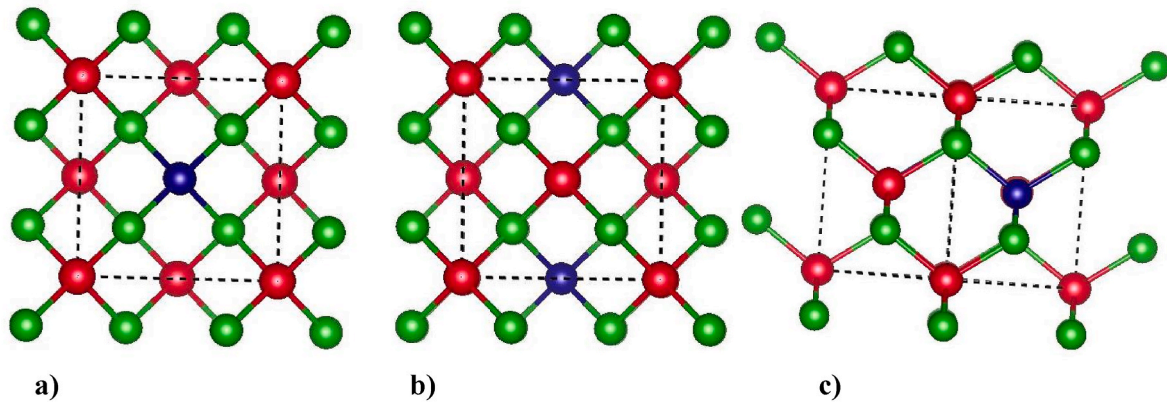

Fig. 2. Crystal structure of $Zn_{0.25}Cd_{0.75}Te$ in a) a-b plane, b) b-c or a-c plane, and c) [111] direction. Green, blue, and red balls represent Te, Zn and Cd atoms respectively. Dotted line represents single unit cell. These figures are drawn by using Visualization for Electronic and STructural Analysis (VESTA) [143]. (For interpretation of the references to colour in this figure legend, the reader is referred to the Web version of this article.)

with respect to the thickness of the thin films of $Zn_xCd_{1-x}Te$ deposited at various substrates as described by Chander et al. [14,15].

Another electronic property affected by alloying is the carrier effective mass (m^*) which influences the photo-current and ultimately the efficiency of the solar cells. The electron effective masses (m_e^*) for the end members CdTe and ZnTe are calculated to be 1.33 m_o and 1.20 m_o, where m_o is the electron rest mass. There is an upward bowing in m_e^* with the bowing parameter $\delta_{m_e^*}$ to be -1.69 m_o. Similarly, the hole effective mass (m_h^*) for the end members CdTe and ZnTe are calculated to be both 0.17 m_o. There is an upward bowing in m_h^* with the bowing parameter $\delta_{m_e^*}$ to be -0.96 m_o. This upward bowing in both effective masses (shown in Fig. 1b) are not benevolent to the efficiency of the solar cells. Further study of other electronic parameters must be done to mitigate this rise in the masses. Overall, electron masses are higher in all the members of $Zn_xCd_{1-x}Te$ than holes. It could be because $Zn_xCd_{1-x}Te$ is of a p-type semi-conductor. Our choice of the photovoltaic absorber $Zn_{0.25}Cd_{0.75}Te$ has m_e^* 4.46 times heavier than m_h^*. Besides the average effective masses of all the band propagations, we have reported the standard deviation of them as well. All the five members of $Zn_xCd_{1-x}Te$ have standard deviation of the effective masses lower than the average. As discussed already

multiple times, the bowing in carrier effective masses also can be attributed to alloying.

We next studied the charge transferred from cation to the anion in the alloy. Table S4 shows the charge transferred from Cd and Zn to Te in $Zn_xCd_{1-x}Te$ alloys. We observe that the charge transferred to Te from Cd and Zn were calculated to be 0.52 e and 0.50 e in the end members, where e is the elementary charge. Hence, Cd is seen to transfer more charge than Zn in the ordered material because the difference in the electronegativities in the Cd–Te pairs is larger than in Zn–Te pairs which makes the former pair stronger than the latter as discussed in the earlier paragraph [123]. However, in the alloy, we find that Zn transfers more charge than Cd because the Zn has to make its otherwise weaker bond stronger with Te than in the end member ZnTe in order to stabilize in the tetrahedra in the alloys. There is no bowing in the values of these charge transfers but a gradual decrement or increment as the composition changes. Additionally, the study of the charge transfer helps us to identify the type of the bonding taking place between the cation and the anion. As the charge transfer here have been observed to be lesser than 1 e, the bonding is covalent in nature.

Although we have not calculated detailed band structure figure for the alloys due to prohibitive computational cost, we have calculated

projected density of states (PDOS) and projected Crystal Orbital Hamilton Population (pCOHP) vs. Energy to visualize the electronic properties of the alloys. They are shown in Figures S3 and S4 respectively. From PDOS figure, we can assert that Te p-orbital is more pronounced than any other orbital below the Fermi level in the $Zn_xCd_{1-x}Te$ alloy system. Besides Te p-orbital, Zn d- and Cd d-orbitals seem to influence the DOS below the Fermi level. However, above the Fermi level, Te-p orbital is seen equally dominant along with Zn s- and Cd s-orbitals. This is consistent with the highest electronegativity of Te while compared to Zn and Cd [123]. The states start to appear in the figure after the bandgap above the Fermi level which confirms the non-metallic behavior of the alloy system. Our trends on DOS have been consistent with earlier theoretical work [12,37]. Figure S4 for pCOHP also augments this finding. Besides such finding, pCOHP figure has peaks related to bonding below the Fermi level at those places where we had observed peaks in PDOS exactly at those venue for different orbitals simultaneously. Also, the anti-bonding area above the Fermi level in the pCOHP figure signifies the loosely held electrons in the conduction band.

Finally, we studied optical properties of disordered $Zn_xCd_{1-x}Te$ alloy system. As the B3 structure is a cubic crystal, its interaction with the photons is isotropic. Figure S5 shows complex dielectric function of $Zn_xCd_{1-x}Te$ alloys in visible-UV range whereas Figure S6 shows in the range of (0-15) eV. The first peak of real part of the dielectric function for each stoichiometry is observed at the bandgap. Similarly, the first peak on imaginary part has some positive value and a peak after the bandgap for each stoichiometry. After the first peak, both the real and imaginary parts of the dielectric function display various prominent peaks later. These peaks are due to several inter- and intra-band transitions as well as electronic collisions in the lattice [95]. The dielectric constants for $Zn_xCd_{1-x}Te$ have been tabulated in Table S5 from where we obtain dielectric constants for the end members CdTe and ZnTe are found to be 5.87 and 6.04 respectively. The dielectric constants for intermediate members of $Zn_xCd_{1-x}Te$ create a bowing effect with bowing parameter δ_ε of −2.32 obtained using Eq. (3) with p = ε is shown in Figure S7. This upward bowing increases the values for the intermediate members of the alloy. As compared to Si value of 11.7 [102], these values are lower that compromises the likelihood of charge segregation due to feebly screened columbic attraction ultimately reducing the efficiency of the solar cells [130]. Among the alloy system, $Zn_{0.75}Cd_{0.25}Te$ has the highest value of the dielectric constant. However, as $Zn_{0.25}Cd_{0.75}Te$ has been chosen as a better fit so far for the ideal property of the absorber material, the dielectric value of 6.36 is also comparable to the highest value and hence can act as a better absorber material in solar cells.

Complex dielectric function can be used to derive some crucial physical quantities like absorption coefficient and reflectivity [97] which helps us to comprehend photovoltaic efficiency. Fig. 3a displays absorption coefficient in visible-UV range for $Zn_xCd_{1-x}Te$ alloy system along with standard AM 1.5 G solar spectral irradiance. We observe that the energies at first absorption peaks correlate directly with the electronic bandgaps exactly for each stoichiometry, similar to the complex dielectric function discussed in the previous paragraph. The other trailing peaks are due to the other transitions and electronic collisions in the lattice. The absorption spectra remain relatively unchanged for each stoichiometry. However, they shift towards lower energies for minority Zn concentrations and higher energies for majority corresponding to their bandgaps. Overall, $Zn_xCd_{1-x}Te$ is found to perpetuate a robust optical absorption of the order of 10^4 cm^{-1} [26], which is equivalent to the absorption of widely used photovoltaic material $CdSe_xTe_{1-x}$ alloys [9]. Consistent with the absorption, reflectivity curves shown in Fig. 3b show a similar pattern. Their value range between 0.18 and 0.23 within the bandgap of the material. Specifically for ZnTe, our value of 22.7% reflection at 2.37 eV photon energy matches closely with the experimental result of 20.1% [26]. Above the bandgap within the visible-UV range, although the reflectivity keeps rising showing some peaks, the reflectivity is contained within 0.33. To put in a nutshell, material with
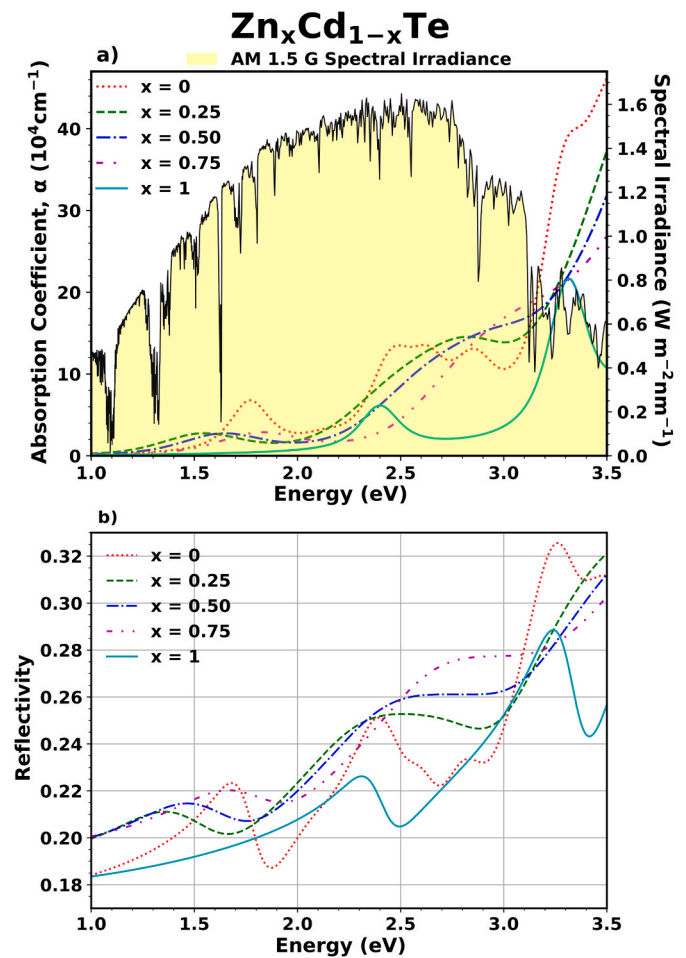

Fig. 3. Absorption coefficient, α (top panel) and reflectivity (bottom panel) curves, left axis, of $Zn_xCd_{1-x}Te$ alloys in B3 crystal structure computed using the hybrid HSE06 functional. Standard AM 1.5 G solar spectral irradiance [144], right axis, is illustrated in the yellow shaded area along with absorption curve. (For interpretation of the references to colour in this figure legend, the reader is referred to the Web version of this article.)

this absorptivity and reflectivity, $Zn_xCd_{1-x}Te$ alloy system can be used as graded absorber layers, or in particular, $Zn_{0.25}Cd_{0.75}Te$ can act as the best absorber layer in solar cells to achieve a higher efficiency.

Charge carrier mobility, Urbach Energy, and exciton binding energy of $Zn_xCd_{1-x}Te$ alloys are displayed in Table S6. As the charge carrier mobility is inversely proportional to the effective masses, electron mobility is lower than hole mobility. The charge carrier mobility in the intermediate members is lesser than in the end members of the alloys due to the extra scattering in the alloys. All the charge carrier mobility values are lesser than that for silicon at room temperature (Electron mobility: 1350 cm^2/Vs, Hole mobility: 480 cm^2/Vs) [102]. Calculated hole mobilities for CdTe and ZnTe match with earlier experimental work [131,132]. The Urbach energy in the $Zn_xCd_{1-x}Te$ alloys is roughly linearly increasing with Zn concentration. Their values are below the thermal energy of room temperature (approx. 25 meV), which are considered favorably low for photovoltaic action which does not substantially reduce open circuit voltage (V_{OC}) [133]. Our value of Urbach energy of 18.94 meV closely matches with the experimental value of 15 meV for CdTe [133]. The exciton binding energy increases first with the Zn concentration and decreases later. All the values of exciton binding energy for $Zn_xCd_{1-x}Te$ alloys are below 100 meV which is considered optimal for solar cells [103] that helps to increase efficiency of solar cells by increasing short circuit current density (J_{SC}).

3.2. Phase equilibrium of Zn$_x$Cd$_{1-x}$Te

To understand the phase equilibria of Zn$_x$Cd$_{1-x}$Te alloy system, we have computed formation energy landscape and phase diagram using cluster expansion formalism [81]. The accuracy of our computations can be established from a very small cross-validation score of 0.8 meV. Formation energy landscape of Zn$_x$Cd$_{1-x}$Te is displayed in Fig. 4. The upward bowing in the formation energy landscape suggests endothermic mixing in the alloy, consistent with our discussion on formation energy on section 3.1. The rise in the enthalpy can be as high as 39 meV for 50% Zn concentration. Due to the difference in covalent radii (130.4 p.m. and 148.2 p.m. for Zn and Cd respectively), the landscape displays a small skewness towards CdTe. The skewness observed in ternary alloys has been widely studied which can be attributed to volume change, chemical exchange, and relaxation [63].

Temperature-concentration (T-x) phase diagram for Zn$_x$Cd$_{1-x}$Te system is presented in Fig. 5. Phase segregation is thermodynamically observable for all concentrations at lower temperatures due to the endothermic mixing conditions just discussed. By the addition of vibrational and configurational contribution to the entropy, the consolute temperature decreases to 387 K from 410 K at 40% Zn concentration. Using other theoretical techniques, such as using LDA, Onda-Ito model and quasi-chemical approximations, others have obtained the consolute temperature for this alloy system in the range of (460 − 701) K at (43− 62.3)% Zn concentration [134–136]. In some of the reported experimental work performed at various concentrations ($0 \leq x \leq 1$), the preparation temperatures have been in the range of (773 − 900) K [137, 138]. There has been no experimental work reporting the consolute temperature. Our values of consolute temperature remain predictive and experimental verification is suggested. As our work includes both vibrational and configurational contribution to the entropy, it predicts a lower consolute temperature than previous work and is thus expected to be more accurate [134–136].

3.3. Short-range order (SRO) effects

Since there are two different atoms in the cationic sublattice of 4a Wyckoff positions, the intermediate members of the Zn$_x$Cd$_{1-x}$Te alloy system have cationic disorder, and significant SRO is observed in these disordered materials. As we have established from our discussion so far that Zn$_{0.25}$Cd$_{0.75}$Te has better photovoltaic properties (e.g., right band gap) within the Zn$_x$Cd$_{1-x}$Te alloy system, we studied the effects of SRO

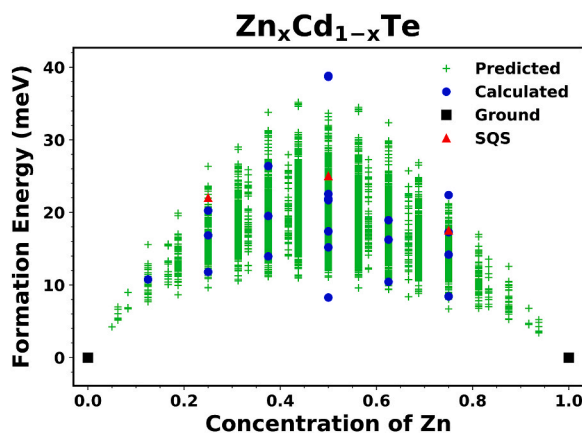**Fig. 4.** Energy landscape of Zn$_x$Cd$_{1-x}$Te in B3 crystal structure displaying intermediate states predicted (green crosses) through cluster expansion and calculated (blue circles) using DFT, ground states (black squares) of CdTe and ZnTe, and special quasirandom structures (SQS) (red triangles) simulated at concentrations of x = 0.25, 0.50, 0.75. (For interpretation of the references to colour in this figure legend, the reader is referred to the Web version of this article.)
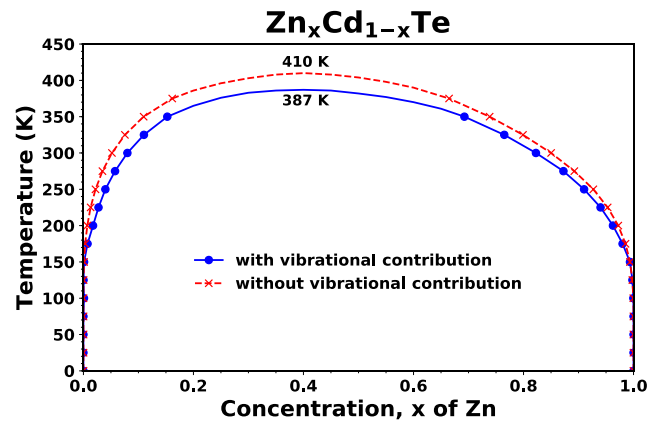

Fig. 5. Temperature-concentration (T-x) phase diagram of Zn$_x$Cd$_{1-x}$Te generated from Monte Carlo simulations utilizing effective cluster interaction coefficients. Red crosses (without vibrational contribution) and blue circles (with vibrational contribution) are the calculated data whereas the lines are interpolations and extrapolations of the calculated data. The consolute temperature of alloying solid solution is predicted to be 387 K. Calculation without vibrational contribution to the phase diagram predicted a higher consolute temperature of 410 K. (For interpretation of the references to colour in this figure legend, the reader is referred to the Web version of this article.)

for that composition (x = 0.25). Fig. 6a presents frequency of occurrences of all possible Zn–Cd coordination numbers relative to their completely random configuration simulated in 1728-atom supercells. We observe that the frequency of Zn–Cd coordination number at coordination numbers 1, 2, 3, 10, 11 and 12 is higher whereas at the rest of the coordination numbers is lesser at 400 K. This distribution of the coordination numbers leads us to a negative value of −0.79 of SRO parameter as defined in Eq. (2). Also, from Eq. (2), we can clearly identify that if the total number of bonds in the alloy (N^{Zn-Cd}) is higher than in the random limit (N_{random}^{Zn-Cd}), the SRO parameter becomes negative. Although the distribution in Fig. 6a displays a lesser number of bonds in the intermediate coordination numbers at 400 K than in the random limit, the total sum of the number of bonds in all the coordination numbers is higher as we see a greater number of bonds in other coordination numbers. This effect is considered as "anti-clustering" that defines the bonding of different atoms i.e., Zn and Cd in the same sublattice [139]. This "anti-clustering" effect proceeds towards the "clustering", meaning the bonding of similar atoms i.e., Zn and Zn or Cd and Cd in the same sublattice, at higher temperatures as revealed from increasing value of the SRO parameter. Fig. 6c shows such variation of the SRO parameter with temperature. It is clear from the figure that the parameter increases with increasing temperature. Again, from Fig. 6a, we can see that the distribution of the coordination numbers is less dispersed at 1000 K than at 400 K, hence has a positive value of 0.11 of SRO parameter i.e., clustering is observed.

Fig. 6b displays the bond angle distribution of ∡ZnTeCd in the Zn$_{0.25}$Cd$_{0.75}$Te alloy at two different temperatures. We notice a smaller width of bond angle distribution at 400 K than at 1000 K. Along with the distribution, we also calculated their bandgaps using the GGA pseudopotential, to compare the effect of structural distortion on bandgap. We have found that the bandgap is slightly higher at 1000 K (1.07 eV) than at 400 K (1.02 eV). This can be attributed to the lower median value of bond angle distribution that signifies greater strain on the bond and subsequent increase in the bandgap. Though very minor in the magnitude of change, this change in bandgap due to the difference in bond angle distributions are consistent with similar finding of Huang et al. [140]. For such a large temperature different of 600 K, the difference in the gap can be considered low, however it opens the possibility of bandgap engineering. Experimentally, the fine tuning of bandgap can be
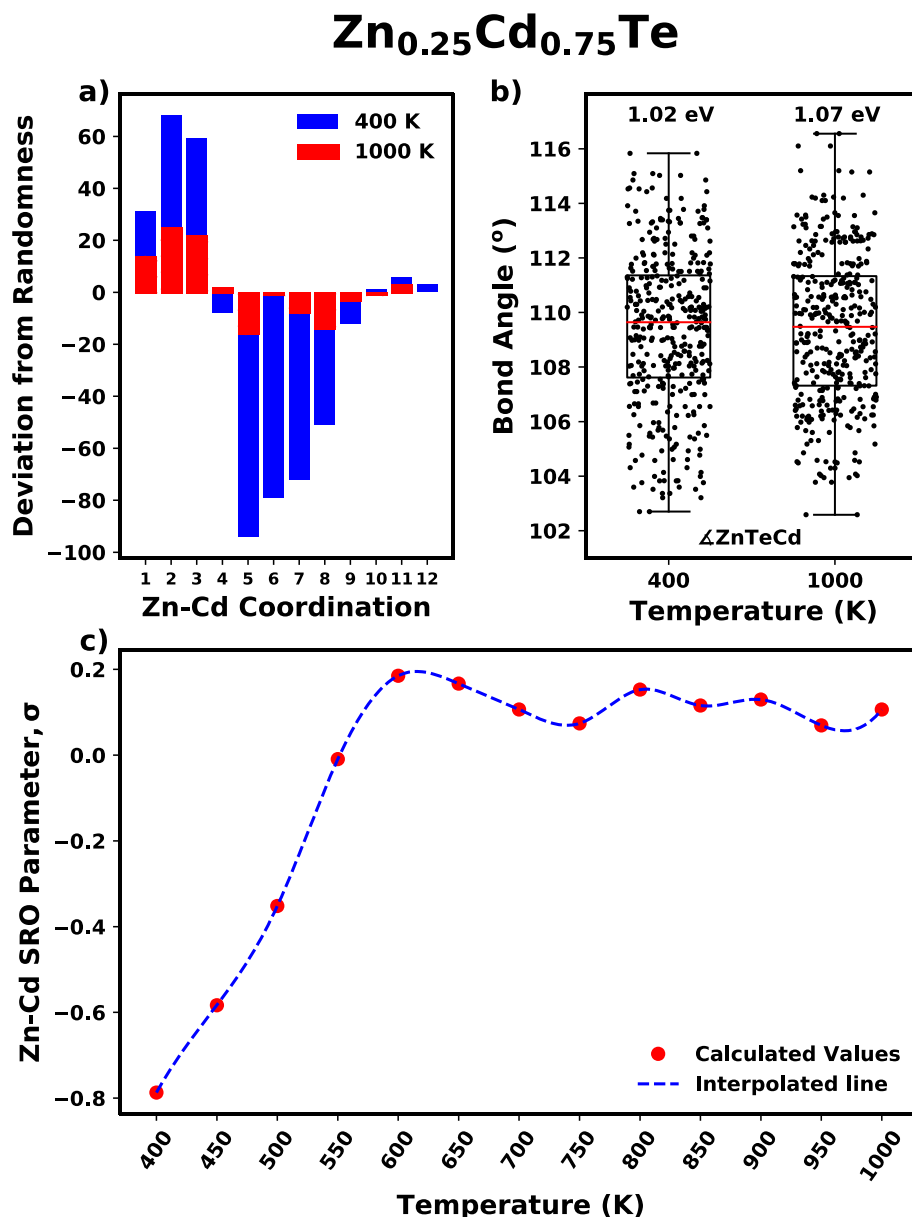
Zn$_{0.25}$Cd$_{0.75}$Te

Fig. 6. a) Frequency of occurrences of all possible Zn–Cd coordination numbers relative to their completely random configuration. Values here are taken from 1728-atom supercells. b) Bond angle distributions of ∡ZnTeCd in Zn$_{0.25}$Cd$_{0.75}$Te simulated at 400 K and 1000 K. Also, bandgaps in those distributions are provided in eV calculated using GGA. c) Short-range order parameter, σ defined in Eq. (2), of Zn–Cd pairs in the cation sublattice of disordered Zn$_{0.25}$Cd$_{0.75}$Te simulated at various temperatures. Negative values imply a deficiency of Zn–Te bonds relative to the random limit.

achieved by controlling the degree of clustering during the synthesis process in the corresponding temperature and quenching in order to preserve the local occupation within the structure [141]. This discussion adds temperature processing as a parameter to our discussion of bandgap engineering with composition from section 3.1.

4. Conclusion

We have done a thorough investigation of Zn$_x$Cd$_{1-x}$Te alloy system in its structural, optical, and electronic front. The alloy is found to be endothermic owing to the strain due to the accommodation of two different atoms Zn and Cd of differing covalent radii. This effect can also be attributed to the bond length and bond angle distribution observed in this system. Especially, the bond length between cation and anion in the alloy was found to significantly vary than in the binary crystals. Downward bowing is observed in the bandgap implying Zn$_{0.25}$Cd$_{0.75}$Te with the minimum bandgap of 1.49 eV in the system is promising for photovoltaic application. Moreover, additional work on the defects of Zn$_{0.25}$Cd$_{0.75}$Te, such as vacancies of Zn, Cd or Te, interstitials, anti-site defects, substitution, dislocation, grain orientation, etc. will help to

understand the material further. Zn$_x$Cd$_{1-x}$Te alloy system can be used to deposit graded layers to capture a large fraction of the solar spectrum. There is an upward bowing in both hole and electron effective masses. The result of small charge transfer suggests that the computations are consistent with the covalent bonding in these semi-conductors. Also, Zn transfers more charge to the Te than Cd consistent with their electronegativities. Electronic states are found to be positively bonded below the Fermi level whereas negatively bonded above the Fermi level as observed in DOS and pCOHP analyses. Also, Te electronic states were dominant over Zn and Cd below the Fermi level whereas comparable above the Fermi level. The dielectric constants have an upward bowing in the system that highly improves charge segregation for better carrier transport. The energies at the first absorption peaks were found to correlate directly with the electronic bandgaps for each stoichiometry. The absorption in the alloy is robust of the order of 10^4 cm^{-1}. Reflectivity ranges between 0.18 and 0.23 within the bandgap of the material suggesting minimal reflection. By implementing cluster expansion formalism with both configurational and vibrational contribution to the entropy, we have obtained the consolute temperature for the solid solution to be 387 K at 40% Zn concentration. We saw an association of

different cations at a lower temperature in the alloy than in the random limit known as "anti-clustering" at lower temperatures. This caused a negative value in SRO parameter that moved towards zero or positive at higher temperatures. A lesser width of bond angle distribution at 400 K is observed than at 1000 K. The computed bandgap is slightly higher at 1000 K (1.07 eV) than at 400 K (1.02 eV). Charge carrier mobility, Urbach Energy, and exciton binding energy of $Zn_xCd_{1-x}Te$ alloys are also calculated. Our results indicate temperature as well as composition as possible parameters for bandgap engineering in this system.

Disclaimer

The views and conclusions contained herein are those of the authors and should not be interpreted as necessarily representing the official policies or endorsements, either expressed or implied, of Air Force Research Laboratory or the U.S. Government.

CRediT authorship contribution statement

B.B. Dumre: Writing – review & editing, Writing – original draft, Visualization, Validation, Supervision, Software, Resources, Project administration, Methodology, Investigation, Formal analysis, Data curation, Conceptualization. **R.J. Ellingson:** Writing – review & editing, Funding acquisition, Formal analysis. **S.V. Khare:** Writing – review & editing, Visualization, Validation, Supervision, Software, Resources, Project administration, Investigation, Funding acquisition, Formal analysis, Conceptualization.

Declaration of competing interest

The authors declare that they have no known competing financial interests or personal relationships that could have appeared to influence the work reported in this paper.

Data availability

Data will be made available on request.

Acknowledgement

Appendix A. Supplementary data

Supplementary data related to this article can be found at https ://doi.org/10.1016/j.solmat.2022.111971.

References

[1] M.A. Green, et al., Solar cell efficiency tables (Version 55), Prog. Photovoltaics Res. Appl. 28 (1) (2020) 3–15.

[2] F.K. Alfadhili, et al., *Development of CdCl₂ Activation to minimize Zn Loss from sputtered Cd₁₋ₓZnₓTe thin Films for Use in tandem solar cells*, MRS Adv. 3 (52) (2018) 3129–3134.

[3] K.E.N. Zweibel, Toward low cost CdTe PV, Int. J. Sol. Energy 12 (1–4) (1992) 285–292.

[4] W. Shockley, H.J. Queisser, Detailed balance limit of efficiency of p-n junction solar cells, J. Appl. Phys. 32 (3) (1961) 510–519.

[5] G.M. Wilson, et al., The 2020 photovoltaic technologies roadmap, J. Phys. Appl. Phys. 53 (49) (2020) 493001.

[6] N.R. Paudel, Y. Yan, Enhancing the photo-currents of CdTe thin-film solar cells in both short and long wavelength regions, Appl. Phys. Lett. 105 (18) (2014) 183510.

[7] M. Terheggen, et al., Analysis of bulk and interface phenomena in CdTe/CdS thin-film solar cells, Interface Sci. 12 (2–3) (2004) 259–266.

[8] N. Romeo, et al., Recent progress on CdTe/CdS thin film solar cells, Sol. Energy 77 (6) (2004) 795–801.

[9] B.B. Dumre, et al., Improved optoelectronic properties in CdSeₓTe₁₋ₓ through controlled composition and short-range order, Sol. Energy 194 (2019) 742–750.

[10] T.A.M. Fiducia, et al., Understanding the role of selenium in defect passivation for highly efficient selenium-alloyed cadmium telluride solar cells, Nat. Energy 4 (6) (2019) 504–511.

[11] A.H. Munshi, et al., Polycrystalline CdSeTe/CdTe absorber cells with 28 mA/cm2 short-circuit current, IEEE J. Photovoltaics 8 (1) (2018) 310–314.

[12] I. Khan, et al., First principle optoelectronic studies of visible light sensitive CZT, Superlattice. Microst. 63 (2013) 91–99.

[13] J.-H. Yang, et al., Electronic structure and phase stability of MgTe, ZnTe, CdTe, and their alloys in the B3, B4, and B8 structures, Phys. Rev. B 79 (24) (2009) 245202.

[14] S. Chander, M.S. Dhaka, Effect of thickness on physical properties of electron beam vacuum evaporated CdZnTe thin films for tandem solar cells, Phys. E Low-dimens. Syst. Nanostruct. 84 (2016) 112–117.

[15] S. Chander, et al., Effect of substrates on structural, optical, electrical and morphological properties of evaporated polycrystalline CdZnTe thin films, Phys. E Low-dimens. Syst. Nanostruct. 89 (2017) 29–32.

[16] P.P. Gunaicha, et al., *Structural, energetic and elastic properties of Cu₂ZnSn(SₓSe₁₋ₓ)₄ (x= 1, 0.75, 0.5, 0.25, 0) alloys from first-principles computations*, Sol. Energy 102 (2014) 276–281.

[17] S. Zhang, et al., Characterization of the microstructures and optical properties of CdTe(0 0 1) and (1 1 1) thin films grown on GaAs(0 0 1) substrates by molecular beam epitaxy, J. Cryst. Growth 546 (2020) 125756.

[18] X.C. Cai, et al., Spectroscopy of CdTe/CdSe type-II nanostructures: morphology, lattice mismatch, and band-bowing effects, J. Phys. Chem. C 116 (14) (2012) 8118–8127.

[19] T.A. Gessert, et al., Research strategies toward improving thin-film CdTe photovoltaic devices beyond 20% conversion efficiency, Sol. Energy Mater. Sol. Cell. 119 (2013) 149–155.

[20] J. Perrenoud, et al., A comprehensive picture of Cu doping in CdTe solar cells, J. Appl. Phys. 114 (17) (2013) 10.

[21] R.M. Geisthardt, M. Topic, J.R. Sites, Status and potential of CdTe solar-cell efficiency, IEEE J. Photovoltaics 5 (4) (2015) 1217–1221.

[22] J. Sites, et al., Progress and challenges with CdTe cell efficiency, in: 2016 IEEE 43rd photovoltaic specialists conference (PVSC), 2016.

[23] A. Polman, et al., Photovoltaic materials: present efficiencies and future challenges, Science 352 (6283) (2016) p. aad4424.

[24] J. Orton, P. Blood, The electrical characterization of semiconductors: majority carriers and electron states, 1992.

[25] W. Shockley, W.T. Read, Statistics of the recombinations of holes and electrons, Phys. Rev. 87 (5) (1952) 835–842.

[26] O. Oklobia, G. Kartopu, S.J.C. Irvine, Properties of arsenic–doped ZnTe thin Films as a back Contact for CdTe solar cells, Materials 12 (22) (2019) 3706.

[27] W. Nan, et al., Crystal structure control of zinc-blende CdSe/CdS core/shell nanocrystals: synthesis and structure-dependent optical properties, J. Am. Chem. Soc. 134 (48) (2012) 19685–19693.

[28] M. Koç, G. Kartopu, S. Yerci, *Combined optical-electrical Optimization of Cd₁₋ₓZnₓTe/silicon tandem solar cells*, Materials 13 (8) (2020) 1860.

[29] C. Li, et al., Identification of deep level defects in CdTe solar cells using transient photo-capacitance spectroscopy, Jpn. J. Appl. Phys. 60 (SB) (2020) p. SBBF01.

[30] F.K. Alfadhili, et al., Back-Surface Passivation of CdTe solar cells using solution-processed oxidized aluminum, ACS Appl. Mater. Interfaces 12 (46) (2020) 51337–51343.

[31] K.K. Subedi, et al., Semi-transparent p-type barium copper sulfide as a back contact interface layer for cadmium telluride solar cells, Sol. Energy Mater. Sol. Cell. 218 (2020) 110764.

[32] N. Amin, A. Yamada, M. Konagai, Effect of ZnTe and CdZnTe Alloys at the back Contact of 1-μm-Thick CdTe thin film solar cells, Jpn. J. Appl. Phys. 41 (Part 1, No. 5A) (2002) 2834–2841.

[33] B. Späth, et al., Nitrogen doping of ZnTe and its influence on CdTe/ZnTe interfaces, Appl. Phys. Lett. 90 (6) (2007) 62112.

[34] G. Zha, et al., The growth and the interfacial layer of CdZnTe nano-crystalline films by vacuum evaporation, Vacuum 86 (3) (2011) 242–245.

[35] T.L. Chu, et al., Films and junctions of cadmium zinc telluride, J. Appl. Phys. 71 (11) (1992) 5635–5640.

[36] S. Chander, M.S. Dhaka, Physical properties of vacuum evaporated CdTe thin films with post-deposition thermal annealing, Phys. E Low-dimens. Syst. Nanostruct. 73 (2015) 35–39.

[37] H. Duan, et al., *Composition-dependent electronic properties, optical transitions, and anionic relaxations of Cd₁₋ₓZnₓTe alloys from first principles*, Phys. Rev. B 76 (3) (2007) 35209.

[38] H. Duan, et al., First-principles study of fundamental properties and electronic structure of Cd1–xZnxTe alloys, Phys. Lett. 370 (5) (2007) 517–521.

[39] J.M. Sanchez, F. Ducastelle, D. Gratias, Generalized cluster description of multicomponent systems, Phys. Stat. Mech. Appl. 128 (1–2) (1984) 334–350.

[40] F. Ducastelle, F. Ducastelle, Order and phase stability in alloys, 1991.

[41] D. De Fontaine, Cluster approach to order-disorder transformations in alloys, Solid State Phys. (1994) 33–176. Elsevier.

[42] A. Zunger, First-principles statistical mechanics of semiconductor alloys and intermetallic compounds, in: Statics and Dynamics of Alloy Phase Transformations, Springer, 1994, pp. 361–419.

[43] M. Newman, G. Barkema, Monte Carlo Methods in Statistical Physics Chapter 1-4, Oxford University Press, New York, USA, 1999.

[44] K.B.a.D. Heermann, Monte Carlo Simulation in Statistical Physics, Springer-Verlag, New York, 1988.

[45] B. Dünweg, D. Landau, Phase diagram and critical behavior of the Si-Ge unmixing transition: a Monte Carlo study of a model with elastic degrees of freedom, Phys. Rev. B 48 (19) (1993) 14182.

[46] M. Laradji, D. Landau, B. Dünweg, Structural properties of $Si_{1-x}Ge_x$ alloys: a Monte Carlo simulation with the Stillinger-Weber potential, Phys. Rev. B 51 (8) (1995) 4894.

[47] S.V. Khare, T.L. Einstein, N.C. Bartelt, Dynamics of step doubling: simulations for a simple model and comparison with experiment, Surf. Sci. 339 (3) (1995) 353–362.

[48] G. Kresse, J. Furthmuller, Efficiency of ab-initio total energy calculations for metals and semiconductors using a plane-wave basis set, Comput. Mater. Sci. 6 (1) (1996) 15–50.

[49] G. Kresse, J. Hafner, Ab initio molecular dynamics for liquid metals, Phys. Rev. B 47 (1) (1993) 558–561.

[50] G. Kresse, J. Furthmuller, Efficient iterative schemes for ab initio total-energy calculations using a plane-wave basis set, Phys. Rev. B 54 (16) (1996) 11169–11186.

[51] G. Kresse, J. Hafner, Ab initio molecular-dynamics simulation of the liquid-metal–amorphous-semiconductor transition in germanium, Phys. Rev. B 49 (20) (1994) 14251.

[52] P.E. Blochl, Projector augmented-wave method, Phys. Rev. B 50 (24) (1994) 17953–17979.

[53] G. Kresse, D. Joubert, From ultrasoft pseudopotentials to the projector augmented-wave method, Phys. Rev. B 59 (3) (1999) 1758–1775.

[54] J.P. Perdew, et al., Atoms, molecules, solids, and surfaces - applications of the generalized gradient approximation for exchange and correlation, Phys. Rev. B 46 (11) (1992) 6671–6687.

[55] J.P. Perdew, et al., Erratum: atoms, molecules, solids, and surfaces: Applications of the generalized gradient approximation for exchange and correlation, Phys. Rev. B 48 (7) (1993) 4978.

[56] K. Balasubramanian, S.V. Khare, D. Gall, Energetics of point defects in rocksalt structure transition metal nitrides: thermodynamic reasons for deviations from stoichiometry, Acta Mater. 159 (2018) 77–88.

[57] B.D. Ozsdolay, et al., *Cubic β-WNx layers: Growth and properties vs N-to-W ratio*, Surf. Coating. Technol. 304 (2016) 98–107.

[58] K. Zhang, et al., Growth and mechanical properties of epitaxial NbN(001) films on MgO(001), Surf. Coating. Technol. 288 (2016) 105–114.

[59] K. Zhang, et al., *Epitaxial NbCxN1−x(001) layers: growth, mechanical properties, and electrical resistivity*, Surf. Coating. Technol. 277 (2015) 136–143.

[60] I. Efthimiopoulos, et al., Universal link of magnetic exchange and structural behavior under pressure in chromium spinels, Phys. Rev. B 97 (18) (2018) 184435.

[61] V. Adhikari, et al., First principles investigation into the phase stability and enhanced hardness of TiN-ScN and TiN-YN alloys, Thin Solid Films 688 (2019) 137284.

[62] Z.T.Y. Liu, et al., Transparency enhancement for $SrVO_3$ by $SrTiO_3$ mixing: a first-principles study, Comput. Mater. Sci. 144 (2018) 139–146.

[63] Z.T.Y. Liu, et al., First-principles phase diagram calculations for the rocksalt-structure quasibinary systems TiN-ZrN, TiN-HfN and ZrN-HfN, J. Phys. Condens. Matter 29 (3) (2017) 11.

[64] I. Khatri, et al., Correlating structure and orbital occupation with the stability and mechanical properties of 3d transition metal carbides, J. Alloys Compd. (2021) 161866.

[65] B. Wang, et al., Bandgap and strain engineering in epitaxial rocksalt structure $(Ti_{0.5}Mg_{0.5})_{1-x}Al_xN(001)$ semiconductors, J. Mater. Chem. C 8 (36) (2020) 12677–12688.

[66] N.J. Szymanski, et al., Unconventional superconductivity in 3d rocksalt transition metal carbides, J. Mater. Chem. C 7 (40) (2019) 12619–12632.

[67] N.J. Szymanski, et al., Dynamical stabilization in delafossite nitrides for solar energy conversion, J. Mater. Chem. 6 (42) (2018) 20852–20860.

[68] A.W. Ghosh, S.V. Khare, Rotation in an asymmetric multidimensional periodic potential due to colored noise, Phys. Rev. Lett. 84 (23) (2000) 5243–5246.

[69] J.L. Roehl, et al., Binding sites and diffusion barriers of a Ga adatom on the GaAs (001)−c(4×4) surface from first-principles computations, Phys. Rev. B 82 (16) (2010) 165335.

[70] A. Jain, et al., Commentary: the Materials Project: a materials genome approach to accelerating materials innovation, Apl. Mater. 1 (1) (2013) 11.

[71] K. Balasubramanian, S. Khare, D. Gall, Vacancy-induced mechanical stabilization of cubic tungsten nitride, Phys. Rev. B 94 (17) (2016) 174111.

[72] J.L. Roehl, S.V. Khare, Diffusion of Cd vacancy and interstitials of Cd, Cu, Ag, Au and Mo in CdTe: a first principles investigation, Sol. Energy 101 (2014) 245–253.

[73] J.L. Roehl, S.V. Khare, Diffusion of Te vacancy and interstitials of Te, Cl, O, S, P and Sb in CdTe: a density functional theory study, Sol. Energy Mater. Sol. Cell. 128 (2014) 343–350.

[74] J.L. Roehl, Z.T.Y. Liu, S.V. Khare, Diffusion in CdS of Cd and S vacancies and Cu, Cd, Cl, S and Te interstitials studied with first-principles computations, Mater. Res. Express 1 (2) (2014) 25904.

[75] J. Warner, et al., Ab initio calculations for properties of MAX phases Ti_2TlC, Zr_2TlC, and Hf_2TlC, Appl. Phys. Lett. 88 (10) (2006) 101911.

[76] X. Zhou, D. Gall, S.V. Khare, Mechanical properties and electronic structure of anti-ReO_3 structured cubic nitrides, M_3N, of d block transition metals M: an ab initio study, J. Alloys Compd. 595 (2014) 80–86.

[77] N.J. Szymanski, et al., Prediction of improved magnetization and stability in $Fe_{16}N_2$ through alloying, J. Appl. Phys. 126 (9) (2019) 93903.

[78] V. Adhikari, et al., First-principles study of mechanical and magnetic properties of transition metal (M) nitrides in the cubic M_4N structure, J. Phys. Chem. Solid. 120 (2018) 197–206.

[79] N.J. Szymanski, et al., Electronic and optical properties of vanadium oxides from first principles, Comput. Mater. Sci. 146 (2018) 310–318.

[80] I.S. Khare, et al., Electronic, optical, and thermoelectric properties of sodium pnictogen chalcogenides: a first principles study, Comput. Mater. Sci. 183 (2020) 109818.

[81] Z.T.Y. Liu, et al., First-principles phase diagram calculations for the carbonate quasibinary systems $CaCO_3$-$ZnCO_3$, $CdCO_3$-$ZnCO_3$, $CaCO_3$-$CdCO_3$ and $MgCO_3$-$ZnCO_3$, Chem. Geol. 443 (2016) 137–145.

[82] A. van de Walle, Multicomponent multisublattice alloys, nonconfigurational entropy and other additions to the Alloy Theoretic Automated Toolkit, Calphad Comput. Coupling Phase Diagrams Thermochem. 33 (2) (2009) 266–278.

[83] A. van de Walle, M. Asta, Self-driven lattice-model Monte Carlo simulations of alloy thermodynamic properties and phase diagrams, Model. Simulat. Mater. Sci. Eng. 10 (5) (2002) 521–538.

[84] A. van de Walle, M. Asta, G. Ceder, The alloy theoretic automated Toolkit: a user guide, Calphad Comput. Coupling Phase Diagrams Thermochem. 26 (4) (2002) 539–553.

[85] A. van de Walle, G. Ceder, Automating first-principles phase diagram calculations, J. Phase Equil. 23 (4) (2002) 348–359.

[86] A. van de Walle, Methods for first-principles alloy thermodynamics, JOM (J. Occup. Med.) 65 (11) (2013) 1523–1532.

[87] A. van de Walle, G. Ceder, The effect of lattice vibrations on substitutional alloy thermodynamics, Rev. Mod. Phys. 74 (1) (2002) 11–45.

[88] A. Zunger, et al., Special quasirandom structures, Phys. Rev. Lett. 65 (3) (1990) 353–356.

[89] N. Jiang, et al., An ab initio computational study of pure Zn_3N_2 and its native point defects and dopants Cu, Ag and Au, Thin Solid Films 564 (2014) 331–338.

[90] Y. Wang, et al., Thermal equation of state of silicon carbide, Appl. Phys. Lett. 108 (6) (2016) 61906.

[91] J. Heyd, G.E. Scuseria, M. Ernzerhof, Hybrid functionals based on a screened Coulomb potential, J. Chem. Phys. 118 (21) (2003) 8207–8215.

[92] A.V. Krukau, et al., Influence of the exchange screening parameter on the performance of screened hybrid functionals, J. Chem. Phys. 125 (22) (2006) 224106.

[93] B.B. Dumre, S.V. Khare, Interrelationship of bonding strength with structural stability of ternary oxide phases of $MgSnO_3$: a first-principles study, Phys. B Condens. Matter 637 (2022) 413896.

[94] J. Paier, et al., Screened hybrid density functionals applied to solids, J. Chem. Phys. 124 (15) (2006) 13.

[95] R. Deng, et al., Optical and transport measurement and first-principles determination of the ScN band gap, Phys. Rev. B 91 (4) (2015) 45104.

[96] B.B. Dumre, D. Gall, S.V. Khare, *Stability, and electronic and optical properties of ternary nitride phases of $MgSnN_2$: a first-principles study*, J. Phys. Chem. Solid. 153 (2021) 110011.

[97] S.P. Ong, et al., Python Materials Genomics (pymatgen): a robust, open-source python library for materials analysis, Comput. Mater. Sci. 68 (2013) 314–319.

[98] F. Urbach, The long-wavelength Edge of photographic Sensitivity and of the electronic Absorption of solids, Phys. Rev. 92 (5) (1953), pp. 1324–1324.

[99] C. Kaiser, et al., A universal Urbach rule for disordered organic semiconductors, Nat. Commun. 12 (1) (2021) 3988.

[100] G.K.H. Madsen, J. Carrete, M.J. Verstraete, BoltzTraP2, a program for interpolating band structures and calculating semi-classical transport coefficients, Comput. Phys. Commun. 231 (2018) 140–145.

[101] G.K.H. Madsen, D.J. Singh, BoltzTraP. A code for calculating band-structure dependent quantities, Comput. Phys. Commun. 175 (1) (2006) 67–71.

[102] C. Kittel, Introduction to Solid State Physics, John Wiley&Sons, New York, 2005 (Inc.).

[103] X.-G. Zhao, et al., Design of lead-free inorganic halide Perovskites for solar Cells via cation-transmutation, J. Am. Chem. Soc. 139 (7) (2017) 2630–2638.

[104] D. Porter, K. Easterling, K. Easterling, Phase Transformations in Metals and Alloys, CRC Press, Boca Raton, 2009.

[105] V.L. Deringer, A.L. Tchougreeff, R. Dronskowski, Crystal orbital Hamilton population (COHP) analysis as projected from plane-wave basis sets, J. Phys. Chem. A 115 (21) (2011) 5461–5466.

[106] S. Maintz, et al., Analytic projection from plane-wave and PAW wavefunctions and application to chemical-bonding analysis in solids, J. Comput. Chem. 34 (29) (2013) 2557–2567.

[107] S. Maintz, et al., LOBSTER: a Tool to extract chemical Bonding from plane-wave based DFT, J. Comput. Chem. 37 (11) (2016) 1030–1035.

[108] S. Maintz, M. Esser, R. Dronskowski, Efficient rotation of local basis functions using real spherical harmonics, Acta Phys. Pol. B 47 (4) (2016) 1165–1175.

[109] G. Henkelman, A. Arnaldsson, H. Jonsson, A fast and robust algorithm for Bader decomposition of charge density, Comput. Mater. Sci. 36 (3) (2006) 354–360.

[110] E. Sanville, et al., Improved grid-based algorithm for Bader charge allocation, J. Comput. Chem. 28 (5) (2007) 899–908.

[111] W. Tang, E. Sanville, G. Henkelman, A grid-based Bader analysis algorithm without lattice bias, J. Phys. Condens. Matter 21 (8) (2009) 84204.

[112] M. Yu, D.R. Trinkle, Accurate and efficient algorithm for Bader charge integration, J. Chem. Phys. 134 (6) (2011) 8.

[113] E. Kasper, et al., Test of Vegard's law in thin epitaxial SiGe layers, J. Cryst. Growth 157 (1) (1995) 68–72.

[114] M.-Z. Huang, W.Y. Ching, Calculation of optical excitations in cubic semiconductors. I. Electronic structure and linear response, Phys. Rev. B 47 (15) (1993) 9449–9463.

[115] N. Korozlu, K. Colakoglu, E. Deligoz, Structural, electronic, elastic and optical properties of $CdxZn1-xTe$ mixed crystals, J. Phys. Condens. Matter 21 (17) (2009) 175406.

[116] J.P. Mangalhara, R. Thangaraj, O.P. Agnihotri, STRUCTURAL, OPTICAL AND PHOTOLUMINESCENCE PROPERTIES OF ELECTRON BEAM EVAPORATED $CdSe_{1-x}Te_x$ FILMS, Sol. Energy Mater. 19 (3–5) (1989) 157–165.

[117] Y. Wu, et al., *Growth of $Cd_{1-x}Zn_xTe$ thin films with high Zn content by close-spaced sublimation*, Vacuum 132 (2016) 106–110.

[118] Y. Wang, et al., Synthesis and optical properties of composition-tunable and water-soluble $Zn_xCd_{1-x}Te$ alloyed nanocrystals, J. Cryst. Growth 308 (1) (2007) 19–25.

[119] L. Vegard, Die Konstitution der Mischkristalle und die Raumfüllung der Atome, Z. Phys. 5 (1) (1921) 17–26.

[120] P. Pyykkö, Additive covalent radii for single-, double-, and triple-bonded molecules and tetrahedrally bonded crystals: a summary, J. Phys. Chem. 119 (11) (2015) 2326–2337.

[121] H.-T. Xu, et al., *$Cd_{1-x}Zn_xTe$ alloys properties studied with the Heyd-Scuseria-Ernzerhof screened hybrid density functional*, J. Infrared Millim. Waves 31 (5) (2012) 411–416.

[122] D. Comedi, R. Kalish, Thermal vibrational amplitudes of constituent atoms and mechanical stability in $Zn_xCd_{1-x}Te$ and $Hg_{1-y}Cd_yTe$, Phys. Rev. B 46 (24) (1992) 15844–15858.

[123] A.L. Allred, E.G. Rochow, A scale of electronegativity based on electrostatic force, J. Inorg. Nucl. Chem. 5 (4) (1958) 264–268.

[124] A.D. Compaan, et al., *PROPERTIES OF PULSED LASER DEPOSITED CdS_xTe_{1-x} FILMS ON GLASS*, MRS Proc. 426 (1996) 367.

[125] W.A. Harrison, Electronic Structure and the Properties of Solids: The Physics of the Chemical Bond, Courier Corporation, 2012.

[126] D. Noda, et al., *$Zn_xCd_{1-x}Te$ epitaxial Growth by remote plasma enhanced MOCVD method*, MRS Online Proc. Libr. 487 (1) (1997) 45–49.

[127] A.H. Reshak, et al., Effect of increasing tellurium content on the electronic and optical properties of cadmium selenide telluride alloys $CdSe_{1-x}Te_x$: an ab initio study, J. Alloys Compd. 509 (24) (2011) 6737–6750.

[128] I. Vurgaftman, J.R. Meyer, L.R. Ram-Mohan, Band parameters for III–V compound semiconductors and their alloys, J. Appl. Phys. 89 (11) (2001) 5815–5875.

[129] N. Tit, I.M. Obaidat, H. Alawadhi, Origins of bandgap bowing in compound-semiconductor common-cation ternary alloys, J. Phys. Condens. Matter 21 (7) (2009) 75802.

[130] K.J.T. Hamam, Organic solar cells based on high dielectric constant materials: an approach to increase efficiency, in: Department of Physics, Western Michigan University: Graduate College at ScholarWorks at Western Michigan University, 2013, p. 107.

[131] I. Turkevych, et al., High-temperature electron and hole mobility in CdTe, Semicond. Sci. Technol. 17 (10) (2002) 1064–1066.

[132] M. Aven, B. Segall, Carrier mobility and shallow impurity states in ZnSe and ZnTe, Phys. Rev. 130 (1) (1963) 81–91.

[133] J. Chantana, et al., Impact of Urbach energy on open-circuit voltage deficit of thin-film solar cells, Sol. Energy Mater. Sol. Cell. 210 (2020) 110502.

[134] S.-H. Wei, L.G. Ferreira, A. Zunger, First-principles calculation of temperature-composition phase diagrams of semiconductor alloys, Phys. Rev. B 41 (12) (1990) 8240.

[135] A. Marbeuf, et al., Thermodynamic analysis of Zn-Cd-Te, Zn-Hg-Te and Cd-Hg-Te: phase separation in $ZnxCd1-xTe$ and $ZnxHg1-xTe$, J. Cryst. Growth 117 (1–4) (1992) 10–15.

[136] P. Letardi, N. Motta, A. Balzarotti, Atomic bonding and thermodynamic properties of pseudo-binary semiconducting alloys, J. Phys. C Solid State Phys. 20 (19) (1987) 2853–2884.

[137] P.P. Moskvin, et al., Coherent phase equilibria in the Zn-Cd-Te system and liquid-phase epitaxy of elastically strained $Zn_xCd_{1-x}Te$ alloy layers, Semiconductors 45 (7) (2011) 837–844.

[138] A.S. Alikhanian, et al., Mass spectrometric study of the CdTe–ZnTe system, J. Cryst. Growth 240 (1–2) (2002) 73–79.

[139] L. Bellaiche, A. Zunger, Effects of atomic short-range order on the electronic and optical properties of GaAsN, GaInN, and GaInAs alloys, Phys. Rev. B 57 (8) (1998) 4425.

[140] T.-H. Huang, et al., Structures, electronic and luminescent properties of Cu(I)-quinoline complex at different temperatures and its application to red light-emitting diode, Inorg. Chim. Acta. 514 (2021) 120008.

[141] H. Ji, et al., Hidden structural and chemical order controls lithium transport in cation-disordered oxides for rechargeable batteries, Nat. Commun. 10 (1) (2019) 592.

[142] O.S. Computer, Available from, https://www.osc.edu/.

[143] K. Momma, F. Izumi, VESTA: a three-dimensional visualization system for electronic and structural analysis, J. Appl. Crystallogr. 41 (3) (2008) 653–658.

[144] N.R.E. Laboratory, Reference Air mass 1.5 spectra, Available from, https://www.nrel.gov/grid/solar-resource/spectra-am1.5.html, 2003.